Scaling law for a buckled elastic filament in a shear flow

Paweł Sznajder,[*] Piotr Zdybel,[*,†] Lujia Liu,[‡] and Maria L. Ekiel-Jeżewska[§]
Institute of Fundamental Technological Research, Polish Academy of Sciences, Pawińskiego 5B, 02-106 Warsaw, Poland

(Received 15 March 2024; accepted 2 August 2024; published 30 August 2024)

We analyze the three-dimensional (3D) buckling of an elastic filament in a shear flow of a viscous fluid at low Reynolds number and high Péclet number. We apply the Euler-Bernoulli beam (elastica) theoretical model. We show the universal character of the full 3D spectral problem for a small perturbation of a thin filament from a straight position of arbitrary orientation. We use the eigenvalues and eigenfunctions for the linearized elastica equation in the shear plane, found earlier by Liu *et al.* [Phys. Rev. Fluids **9**, 014101 (2024)] with the Chebyshev spectral collocation method, to solve the full 3D eigenproblem. We provide a simple analytic approximation of the eigenfunctions, represented as Gaussian wave packets. As the main result of the paper, we derive the square-root dependence of the eigenfunction wave number on the parameter $\tilde{\chi} = -\eta \sin 2\phi \sin^2\theta$, where η is the elastoviscous number and the filament orientation is determined by the zenith angle θ with respect to the vorticity direction and the azimuthal angle ϕ relative to the flow direction. We also compare the eigenfunctions with shapes of slightly buckled elastic filaments with a non-negligible thickness with the same Young's modulus, using the bead model and performing numerical simulations with the precise HYDROMULTIPOLE numerical codes.

DOI: 10.1103/PhysRevE.110.025104

I. INTRODUCTION

The dynamics of elastic filaments in low-Reynolds-number fluid flows were recently intensively investigated [1–4]. The growing interest is related to the progress of experimental techniques in tracing the behavior of biological micro-objects such as the flagella of bacteria or algae, chains of diatoms, actin, and cilia [5–13]. Moreover, the development of modern technology has led to the production of elastic nano- and microfibers with controlled length, width, and Young's modulus [14–16] with wide possibilities for their application.

Therefore, the motion and typical shape deformations of elastic fibers have been studied in various fluid flows [12,17–25], with a special interest in the buckling instability [10,26–33]. In particular, the buckling of elastic filaments in a shear flow at low Reynolds number has been extensively investigated in the literature. In Refs. [34,35], experiments were performed, and the minimum value of the shear rate at which thin filaments can buckle was evaluated from the Euler equation. In Ref. [36], the buckling instability of thin elastic filaments was demonstrated by solving the spectral problem for the Euler-Bernoulli beam confined to the shear plane (i.e., the plane spanned by the flow and the flow gradient directions). In Ref. [37], the spectral problem with perturbations out of the shear plane was analyzed, and it was shown that it is the same as in the compressional flow, as studied earlier in Ref. [38]. In Ref. [39], the three-dimensional buckling of thick fibers in a shear flow was studied experimentally and numerically, and it was shown that the buckling is limited to short times only.

In this work, we investigate the buckling instability of an elastic slender filament in the shear flow. We linearize the elastica model [36,40] around an arbitrary orientation, solve the full three-dimensional spectral problem, and derive a scaling law for the eigenvalues and eigenfunctions. We also compare the results with our numerical simulations of flexible fibers with a nonzero thickness.

The plan of this paper is as follows. In Sec. II, the system is introduced. The elastica equation for a slender elastic filament in shear flow is linearized. The fully three-dimensional (3D) spectral problem for the perturbation growth is reduced to solving a single equation with just one parameter, $\tilde{\chi}$. The eigenvalues and eigenfunctions are presented. Section III contains a simple analytical approximation of the eigenfunctions as Gaussian wave packets that is valid for large values of $\tilde{\chi}$ (i.e., for highly flexible filaments). Within this approximation, it is shown that the characteristic wave number of the most unstable eigenfunctions scales as $\sqrt{\tilde{\chi}}$. In Sec. IV, the dependence of the eigenfunctions on $\tilde{\chi}$ is analyzed. The fast Fourier transform of the filament local curvature is evaluated for the elastica's most unstable eigenfunctions. Conclusions are presented in Sec. V. In Appendix A, the asymptotic expansion is applied to provide the scaling of the eigenvalues and eigenfunctions in a range of very small values of the arclength s. In Appendix B, the difference between the wave number based on shape and its curvature is estimated. In Appendix C, the thickness of an elastic filament is taken into account within the bead model and the multipole method, implemented in

[*]These authors contributed equally to this work.
[†]Contact author: pzdybel@ippt.pan.pl
[‡]Present address: Research Institute of Aero-Engine, Beihang University, Beijing 100191, People Republic of China.
[§]Contact author: mekiel@ippt.pan.pl

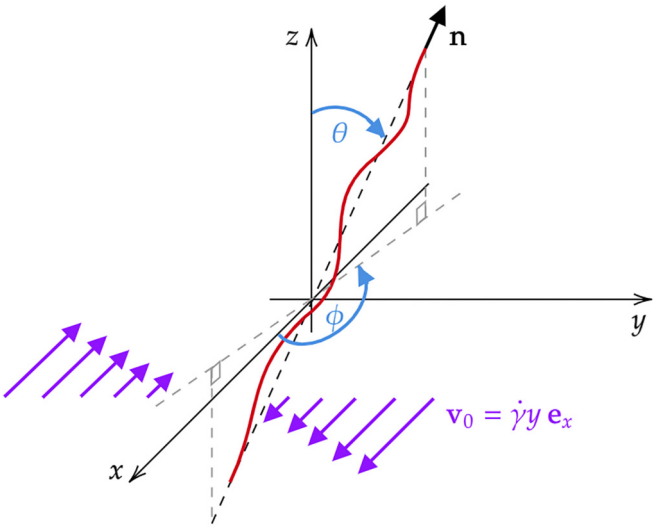

FIG. 1. A schematic of a slender filament in a shear flow.

the HYDROMULTIPOLE numerical code [41,42]. The numerical simulations are performed, and the shapes of the slightly buckled filament are shown and compared with the elastica eigenfunctions.

II. EULER-BERNOULLI BEAM THEORY FOR AN ELASTIC FILAMENT IN A SHEAR FLOW

A. Stability of a small 3D perturbation from a straight configuration

We consider an elastic filament of length L and circular cross section of diameter d under compression of a shear flow

$$\boldsymbol{v}_0 = (\dot{\gamma} y, 0, 0) \tag{1}$$

of a viscous fluid with dynamic viscosity μ. The Reynolds number $\mathrm{Re} \ll 1$, and the Péclet number $\mathrm{Pe} \gg 1$. We assume that the filament aspect ratio is much smaller than unity, $d/L \ll 1$. The elastic forces along the filament are approximated with the use of the Euler-Bernoulli beam theory, as in [2,12,36–38,40,43]. The dimensionless evolution equation, based on resistive force theory [44–46], reads

$$\eta(2\boldsymbol{I} - \boldsymbol{x}_s\boldsymbol{x}_s)\cdot[\boldsymbol{x}_t - \boldsymbol{U}(\boldsymbol{x})] = [T(s,t)\boldsymbol{x}_s]_s - \boldsymbol{x}_{ssss}, \tag{2}$$

where $s \in [-1/2, 1/2]$ is the arclength along the filament centerline, $\boldsymbol{x}(s,t)$ is the position of a filament centerline (both normalized by the filament length L), t is time normalized by $1/\dot{\gamma}$, $\boldsymbol{U} = \boldsymbol{v}_0/(\dot{\gamma}L)$, $T(s,t)$ is the tension, the filament is inextensible (i.e., $\boldsymbol{x}_s \cdot \boldsymbol{x}_s = 1$), and

$$\eta = \frac{2\pi\mu\dot{\gamma}L^4}{EI\ln(2L/d)} \tag{3}$$

is the elastoviscous number, where E is Young's modulus and $I = \pi d^4/64$ is the area moment of inertia (see [36]). The elastoviscous number η estimates the ratio of the hydrodynamic to bending forces. Within the adopted model (2), the dynamics of the filament depends on the aspect ratio and bending stiffness only through η.

As illustrated in Fig. 1, the fiber is almost straight at an arbitrary orientation $\boldsymbol{n}$, determined by the spherical angles $0 < \theta < \pi$ and $\pi/2 < \phi < \pi$ (with the zenith axis along z). There are small perturbations u and v along two unit vectors perpendicular to $\boldsymbol{n}$ and to each other: $\boldsymbol{\lambda}_i$ in the shear plane xy and $\boldsymbol{\lambda}_o$ out of the shear plane, respectively. Therefore,

$$\boldsymbol{x} = s\boldsymbol{n} + u\boldsymbol{\lambda}_i + v\boldsymbol{\lambda}_o. \tag{4}$$

Using the angles, the unit vectors are expressed as

$$\boldsymbol{n} = (\cos\phi\sin\theta, \sin\phi\sin\theta, \cos\theta), \tag{5}$$

$$\boldsymbol{\lambda}_i = (-\sin\phi, \cos\phi, 0), \tag{6}$$

$$\boldsymbol{\lambda}_o = (-\cos\phi\cos\theta, -\sin\phi\cos\theta, \sin\theta). \tag{7}$$

Next, following Ref. [37], we linearize the elastica equation (2) around the straight shape at the orientation $\boldsymbol{n}$. In the zeroth order, the Jeffery equations are recovered [37]. In the first order, the following system of coupled differential equations for the small perturbations u and v is obtained [37]:

$$u_{ssss} + 2\eta u_t + \eta\sin(2\phi)u + \eta\sin(2\phi)\sin^2\theta s u_s + \frac{\eta}{4}\sin(2\phi)\sin^2\theta\left(s^2 - \frac{1}{4}\right)u_{ss} = 0, \tag{8}$$

$$v_{ssss} + 2\eta v_t - \eta\sin(2\phi)\cos^2\theta v + 2\eta\cos(2\phi)\cos\theta u + \eta\sin(2\phi)\sin^2\theta s v_s + \frac{\eta}{4}\sin(2\phi)\sin^2\theta\left(s^2 - \frac{1}{4}\right)v_{ss} = 0. \tag{9}$$

The filament is infinitely thin, so to leading order, the edges do not affect the flow. Therefore, the free boundary conditions at the filament ends are expected [36,37],

$$u_{ss} = u_{sss} = v_{ss} = v_{sss} = 0 \text{ at } s = \pm\tfrac{1}{2}. \tag{10}$$

Then, the spectral method is applied for an arbitrary orientation $\boldsymbol{n}$, assuming that [37]

$$[u, v] = [\Phi_u(s), \Phi_v(s)]\exp(\sigma t), \tag{11}$$

with $\Phi_u(s)$ and $\Phi_v(s)$ being the real in-plane and out-of-plane time-independent shapes and σ being the complex number.

From the linearized equations (8) and (9), the following 3D set of coupled equations for the eigenfunctions $\Phi_u(s)$ and $\Phi_v(s)$ is derived [37]:

$$2\eta\sigma\begin{bmatrix}\Phi_u\\ \Phi_v\end{bmatrix} = \begin{bmatrix}\alpha\hat{\boldsymbol{I}} + \hat{\mathcal{L}} & 0\\ \beta & \alpha'\hat{\boldsymbol{I}} + \hat{\mathcal{L}}\end{bmatrix}\begin{bmatrix}\Phi_u\\ \Phi_v\end{bmatrix} = \begin{bmatrix}\alpha\Phi_u + \hat{\mathcal{L}}\Phi_u\\ \beta\Phi_u + \alpha'\Phi_v + \hat{\mathcal{L}}\Phi_v\end{bmatrix}, \tag{12}$$

$$\hat{\mathcal{L}}(\tilde{\chi}) = -\frac{\partial^4}{\partial s^4} + \tilde{\chi}\left[\frac{1}{4}\left(s^2 - \frac{1}{4}\right)\frac{\partial^2}{\partial s^2} + s\frac{\partial}{\partial s}\right], \tag{13}$$

with $\hat{\boldsymbol{I}}$ being the identity operator and

$$\tilde{\chi} = -\eta\sin(2\phi)\sin^2\theta, \tag{14}$$

$$\alpha = -\eta\sin(2\phi), \tag{15}$$

$$\alpha' = \eta\sin(2\phi)\cos^2\theta, \tag{16}$$

$$\beta = -2\eta\cos(2\phi)\cos\theta. \tag{17}$$

B. Universal character of the spectrum and the eigenfunctions

Equations (12) for the in-plane and out-of-plane perturbations are coupled to each other for $\beta \neq 0$ and decoupled from each other for $\beta = 0$. Generically, there are two cases. Therefore, before giving a general solution to Eq. (12) with $\beta \neq 0$, we first consider the simpler case with $\beta = 0$. It corresponds to $\theta = \pi/2$ (i.e., the filament in the shear plane xy, discussed previously in Ref. [37]) or $\phi = \pi/4$ or $3\pi/4$ (not discussed so far). For $\beta = 0$, the in-plane and out-of-plane perturbations are not coupled, and the set of Eq. (12) has the form

$$2\eta \begin{bmatrix} \sigma_{u1}\Phi_{u1} \\ \sigma_{v1}\Phi_{v1} \end{bmatrix} = \begin{bmatrix} \alpha\Phi_{u1} + \hat{\mathcal{L}}\Phi_{u1} \\ \alpha'\Phi_{v1} + \hat{\mathcal{L}}\Phi_{v1} \end{bmatrix}, \tag{18}$$

with separate eigenvalues σ_{u1} and σ_{v1} and separate eigenfunctions Φ_{u1} and Φ_{v1}.

We recall that after adding to an operator $\hat{\mathcal{L}}$ the identity operator multiplied by any number γ, the eigenvectors Φ_1 remain the same, and γ is added to the eigenvalues λ,[1]

$$(\hat{\mathcal{L}} + \gamma\hat{\boldsymbol{I}})\Phi_1 = (\lambda + \gamma)\Phi_1. \tag{19}$$

Therefore, we can set $\Phi_{v1} = \Phi_{u1}$, and then Eq. (18) can be rewritten as

$$(2\eta\sigma_{u1} - \alpha)\Phi_{u1} = \hat{\mathcal{L}}\Phi_{u1} = (2\eta\sigma_{v1} - \alpha')\Phi_{u1}. \tag{20}$$

In summary, for $\beta = 0$, the sets of in-plane and out-of-plane eigenfunctions are the same, and the in-plane and out-of-plane eigenvalues are shifted in relation to each other by $\alpha' - \alpha$,

$$\sigma_{v1} = \begin{cases} \sigma_{u1} + \frac{\sin(2\phi)}{2} & \text{for} \quad \theta = \pi/2, \\ \sigma_{u1} \pm \frac{(\cos^2\theta + 1)}{2} & \text{for} \quad \phi = \pi/4,\ 3\pi/4. \end{cases} \tag{21}$$

For the unperturbed filament in the shear plane xy, i.e., for $\theta = \pi/2$, the eigenproblem was discussed in Ref. [37]. Reference [37] also pointed out that for $\theta = \pi/2$, the eigenproblem in the shear flow, given by Eq. (18), is the same as that in Ref. [38] for the compressional flow if the parameters are matched to each other accordingly.

However, the full 3D eigenproblem (12) and (13), with coupling between the in-plane and out-of-plane perturbations (i.e., for $\beta \neq 0$), has not been studied so far.

Therefore, now we move on to the 3D system of Eq. (12) for $\beta \neq 0$. In this case, Eq. (12) are coupled with each other. Moreover, the equations for the in-plane perturbation in the systems of equations (18) and (12) are identical, and therefore, $\sigma \equiv \sigma_{u1}$, and $\Phi_u = \Phi_{u1}$. Then we check whether a δ exists such that Φ_u and $\Phi_v = \delta\Phi_u$ are the solution of Eq. (12), which, after applying Eq. (20), take the form

$$2\eta\sigma_{u1} \begin{bmatrix} \Phi_{u1} \\ \delta\Phi_{u1} \end{bmatrix} = \begin{bmatrix} (\alpha + \hat{\mathcal{L}})\Phi_{u1} \\ \beta\Phi_{u1} + 2\eta\sigma_{v1}\delta\Phi_{u1} \end{bmatrix}. \tag{22}$$

The second equation gives the following result for δ:

$$\delta = \frac{\beta}{2\eta\sigma_{u1} - 2\eta\sigma_{v1}} = \frac{\beta}{\alpha - \alpha'} = \frac{2\cos\theta}{\tan(2\phi)(1 + \cos^2\theta)}. \tag{23}$$

[1]By definition, Φ_1 is an eigenvector of an operator $\mathcal{L}$ for an eigenvalue λ iff $\mathcal{L}\Phi_1 = \lambda\Phi_1$.

Therefore, for a given eigenvalue $2\eta\sigma$ of the operator $\alpha\hat{\boldsymbol{I}} + \hat{\mathcal{L}}$, the shape of the out-of-plane eigenfunction Φ_v is the same as the shape of the in-plane eigenfunction Φ_u with the rescaled amplitude.

C. Discussion of the in-plane and out-of-plane perturbations

We showed that for the unperturbed orientation of the fiber out of the shear plane [more specifically, for $\beta \equiv -2\eta\cos(2\phi)\cos\theta \neq 0$], the buckling instability threshold for the growth of both in-plane and out-of-plane perturbations is the same: $\tilde{\chi}_c = 153.2$, and both perturbations increase with time at the same rate, determined by the same eigenvalue σ.

For $\beta = 0$ (i.e., when the unperturbed fiber orientation is restricted to the shear plane), the in-plane and out-of-plane perturbations behave differently. The in-plane perturbations were analyzed in Ref. [36], and the calculated threshold $\tilde{\chi}_c$ for the instability and the growth rate σ coincide with our findings for $\beta \neq 0$. However, for $\beta = 0$, the buckling threshold for the out-of-plane perturbations is larger than for the in-plane ones, $\tilde{\chi}_c' = 221.2$, and the growth rate is slower, $\sigma' = \sigma - \tilde{\chi}/(2\eta)$ [37].

D. The basic spectral problem

We now point out that with the explicit form (13) of the operator $\hat{\mathcal{L}}$, the spectral equation (22) depends only on a single parameter, $\tilde{\chi}$,

$$\left\{ -\frac{\partial^4}{\partial s^4} + \tilde{\chi}\left[\frac{1}{4}\left(s^2 - \frac{1}{4} \right)\frac{\partial^2}{\partial s^2} + s\frac{\partial}{\partial s} \right] - \tilde{\chi}\tilde{\sigma} \right\}\Phi_{u1} = 0, \tag{24}$$

where

$$\tilde{\sigma} = \frac{-2(\sigma + \sin(2\phi)/2)}{\sin(2\phi)\sin^2\theta} \tag{25}$$

and we use the free boundary conditions $\frac{\partial^2\Phi_{u1}}{\partial s^2} = \frac{\partial^3\Phi_{u1}}{\partial s^3} = 0$ for $s = \pm 1/2$ [see Eq. (10)].

Equation (24) is identical to the spectral equation for the elastic fiber in a shear flow with only the in-plane perturbations, solved in Ref. [36], and the spectral equation for the elastic fiber in the compressional flow, solved in Ref. [38], if the parameters are matched accordingly.

The eigenproblem (24) and (25) was solved with the Chebyshev collocation method, as described in Refs. [37,47].

The dependence of a few consecutive larger (including the largest) values of $\tilde{\sigma}$ on $\tilde{\chi}$ is shown in Fig. 2, with an enlargement given in Fig. 3(a). Red and blue denote odd [i.e., $\Phi(s) = -\Phi(-s)$] and even [i.e., $\Phi(s) = \Phi(-s)$] eigenfunctions, respectively (compare with the eigenvalues presented in Refs. [36–38]).

In Fig. 3(b), the local curvature of the eigenfunction corresponding to the largest $\tilde{\sigma}$ is also presented with the use of different colors. To evaluate it, we first change the normalization of the eigenfunction, by introducing $\tilde{\Phi}(s) = \Phi(s) \times 10^{-2}$. Such a choice takes into account that the perturbation is much smaller than unity, in agreement with the first-order expansion. The local curvature is defined in the standard way, $\kappa(s) = |\tilde{\Phi}_{u1}''(s)|/\{1 + [\tilde{\Phi}_{u1}'(s)]^2\}^{3/2}$, approximated for small deformations as $|\tilde{\Phi}_{u1}''(s)|$. Next, $\kappa(s)$ is divided by its maximum value along the filament, i.e., by $\max_s \kappa(s)$. Discontinuities, which are visible in Fig. 3(b), appear at the

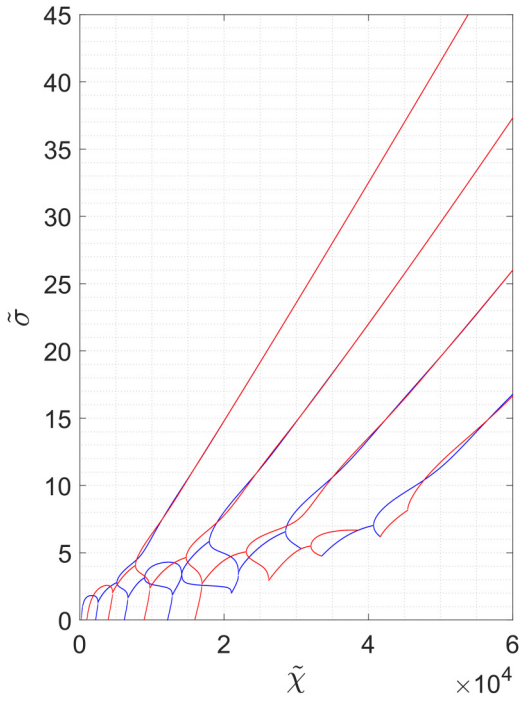

FIG. 2. Solution of the spectral problem (24), taking into account no more than the eight most unstable eigenvalues. Eigenvalues for odd (red) and even (blue) eigenfunctions are shown.

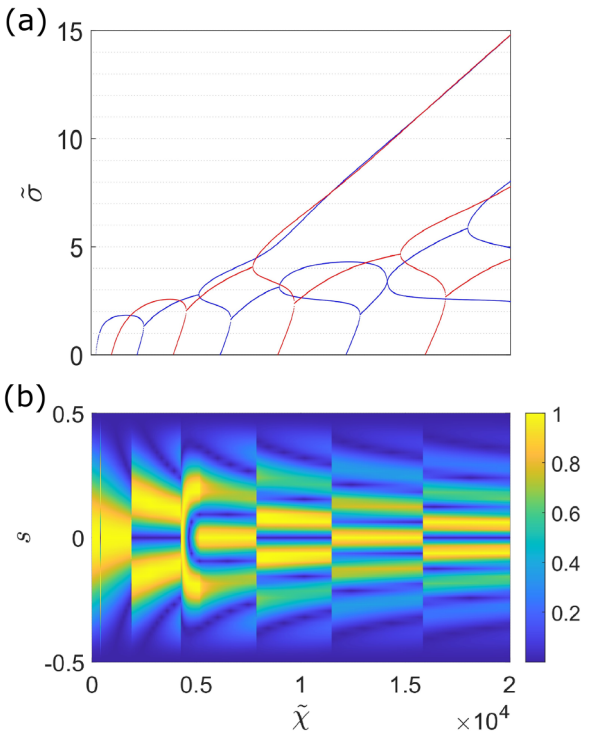

FIG. 3. (a) An enlargement of Fig. 2. (b) The most unstable eigenfunctions. The colors indicate $\kappa(s)/\max_s \kappa(s)$, the local curvature of $\Phi_{u1}(s)$. The range of $\tilde{\chi}$ in both panels is the same.

same values of $\tilde{\chi}$ for which blue and red lines cross each other in the Fig. 3(a), which means that the parity of the most unstable eigenfunction is changed. Such a coupling of the largest odd and the largest even eigenfunctions motivates us to investigate, in Sec. IV B, both of them as continuous functions of $\tilde{\chi}$, similar to what was done in Ref. [38] for the compressional flow.

Figure 2 illustrates that in most cases, the last and next to last eigenvalues correspond to eigenfunctions of a different parity, and therefore, the spectrum degenerates at their crossing point. However, sometimes it happens that the last and next to last eigenvalues correspond to eigenfunctions of the same parity, and they tend to coincide when $\tilde{\chi}$ goes to a certain limiting value (e.g., such a branching point is visible in Fig. 2 at $\tilde{\chi} \approx 5130$).

Those values of $0 \leqslant \tilde{\chi} \leqslant 10^4$ which are the crossing or branching points described above correspond to the borders between the consecutive "modes" shown in Fig. 2 of Ref. [36] for elastica in the shear flow.

The two most unstable eigenfunctions for four different values of $\tilde{\chi}$ are shown in Fig. 4. With the increase of $\tilde{\chi}$, the characteristic wavelength of the oscillations decreases, and the damping of the oscillations is localized closer to $s = 0$.

III. APPROXIMATE ANALYTICAL SOLUTION AT LARGE VALUES OF $\tilde{\chi}$

In this section, we propose a simple analytical approximation of the most unstable eigenvalues and eigenfunctions in Eq. (24) for elastica in a shear flow. We assume that a hydrodynamic forcing dominates the internal bending stiffness of a filament and the elastoviscous number η is large. We restrict

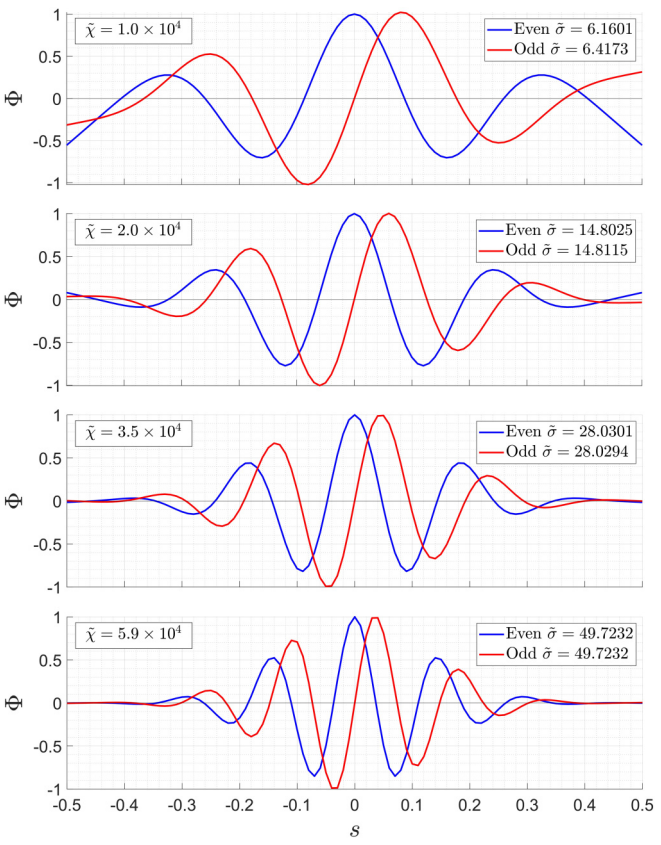

FIG. 4. The eigenfunctions $\Phi(s)$ corresponding to the two most unstable odd and even eigenvalues for four different values of $\tilde{\chi}$. Values of $\tilde{\chi}$ and $\tilde{\sigma}$ are indicated.

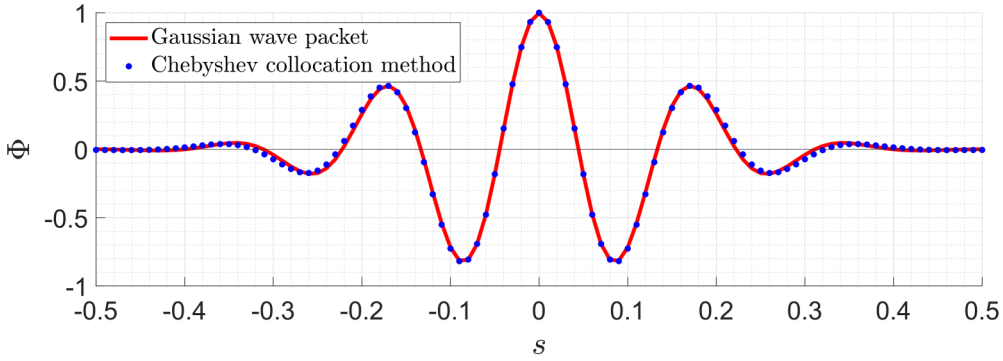

FIG. 5. The eigenfunction Φ as a function of s. Here Φ corresponds to the most unstable eigenvalue for $\tilde{\chi} = 5.4 \times 10^4$. Data depicted by blue dots are computed using the Chebyshev collocation method, and the red line displays the fitted shape of the Gaussian wave packet.

ourselves to angles θ and ϕ such that $\tilde{\chi} = -\eta \sin(2\phi) \sin^2\theta$ is also large. We focus on $\tilde{\chi} \gtrsim 2.5 \times 10^4$ and correspondingly larger values of η [2].

A. Approximation of the shape

An example of the most unstable eigenfunction acquired numerically with the Chebyshev spectral collocation method, as described in Refs. [37,47], is presented in Fig. 5 (blue dots). The numerically received profile of the elastica resembles the Gaussian wave packet. In general, eigenmodes Φ_{u1} are either even or odd functions of the argument s. Thus, we propose an approximate solution $\Phi_{u1} \approx \Phi$ in the form

$$\Phi(s) = \sin(ks)\, e^{\xi s^2} \text{ or } \quad \Phi(s) = \cos(ks)\, e^{\xi s^2}, \tag{26}$$

with $\xi < 0$. This choice is convenient thanks to the evident physical interpretation of parameters k and ξ as a wave number and a measure of dispersion, respectively. Above k is normalized by $1/L$, and in turn, ξ is measured in units of $1/L^2$, where L is the length of the fiber. We fit the expressions (26) to the numerical data obtained via the spectral approach for a wide range of values of $\tilde{\chi} \leqslant 6 \times 10^4$. An example of the fit for $\tilde{\chi} = 5.4 \times 10^4$ is shown in Fig. 5 by the red line. Figure 5 illustrates that discrepancies between the exact shape and its analytical approximation are minuscule, although perceptible close to the ends of the filament. A similar agreement is observed for the whole range of values $2.5 \times 10^4 \leqslant \tilde{\chi} \leqslant 6 \times 10^4$.

B. Scaling of the most unstable eigenfunctions and eigenvalues with $\tilde{\chi}$

Taking advantage of the aforementioned fitting procedure for the most unstable eigenfunctions, we get k and ξ as a function of $\tilde{\chi}$ using data obtained numerically from the Chebyshev collocation method (see [37,47]) for $\tilde{\chi}$ up to 6.0×10^4. We present the results in Fig. 6(a). We notice that for large values of $\tilde{\chi}$, both k and ξ show a linear dependence on $\tilde{\chi}^{1/2}$. The fitting parameters k and ξ are independent. The resulting fits for the range $\tilde{\chi}^{1/2} > 160$ are

$$k = K_1 \tilde{\chi}^{1/2} + K_2, \tag{27}$$

$$\xi = M_1 \tilde{\chi}^{1/2} + M_2, \tag{28}$$

with $K_1 = 0.176 \pm 0.001$, $K_2 = -0.249 \pm 0.003$, $M_1 = -0.124 \pm 0.001$, and $M_2 = 0.417 \pm 0.034$.

In Fig. 2, the most unstable eigenvalue $\tilde{\sigma}$ seems to be linear in $\tilde{\chi}$ for large values of $\tilde{\chi}$. Further examination, illustrated in

[2]Large values of the elastoviscous number are realistic from the point of view of experiments. For example, for actin with a diameter of 8 nm studied in Ref. [12], values of $\eta \approx 2 \times 10^6$ were achieved for actin length $L \approx 20.5\,\mu$m.

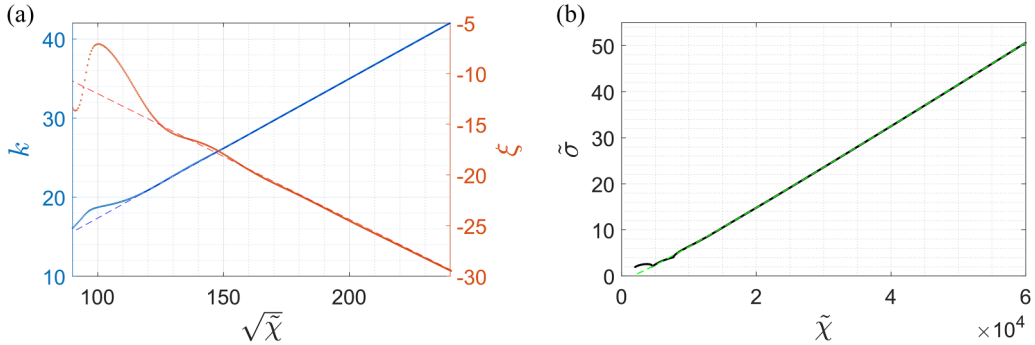

FIG. 6. Scaling of k, ξ, and $\tilde{\sigma}$ with $\tilde{\chi}$. Dots: parameters of the Gaussian wave packet approximation of the eigenfunctions with the most unstable eigenvalue $\tilde{\sigma}$, determined numerically from the Chebyshev collocation method. Dashed lines: fits from Eqs. (27)–(29). (a) The wave number k (blue) and the measure of dispersion ξ (red) vs $\tilde{\chi}^{1/2}$. (b) Dependence of the most unstable eigenvalue $\tilde{\sigma}$ on $\tilde{\chi}$ (black dots and green dashed line).

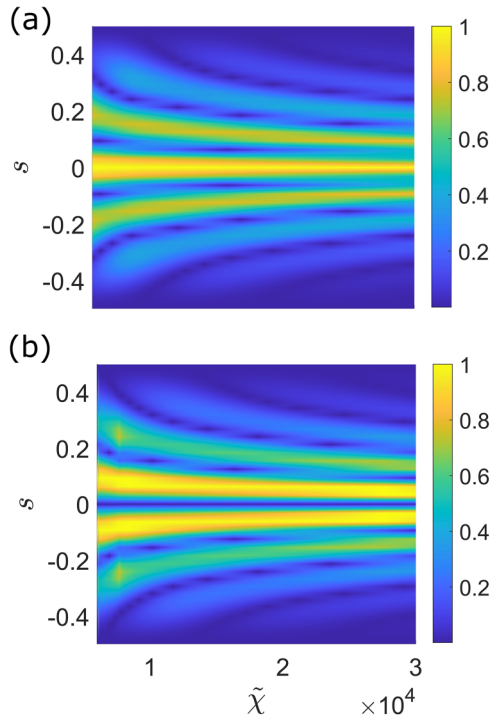

FIG. 7. Local curvature of an elastic filament, normalized by its maximum value along the filament and shown as different colors. Theoretical results for the most unstable (a) even and (b) odd eigenfunctions for the linearized elastica equations.

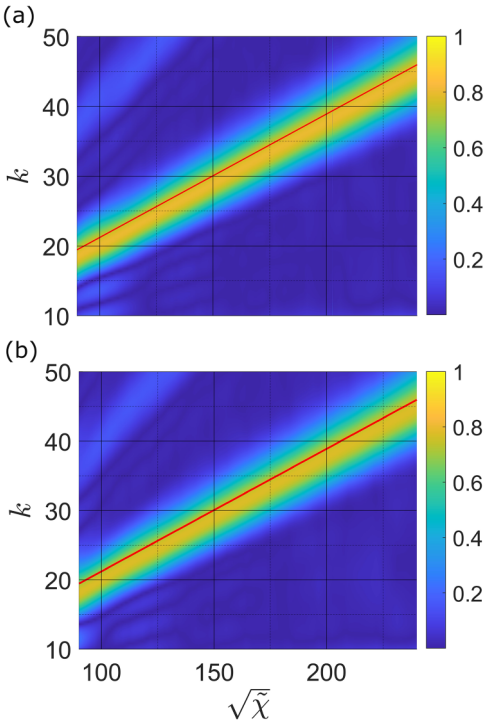

FIG. 8. Wave number k resulting from the fast Fourier transform (FFT) of the local curvature of the elastica most unstable (a) even and (b) odd eigenfunctions vs $\sqrt{\tilde{\chi}}$. The colors indicate the FFT intensity, normalized by its maximum value along the filament. Red line: the scaling (B5) of the local curvature of the approximate Gaussian wave packet, $\alpha_1 \approx \frac{\sqrt{2}}{8}\sqrt{\tilde{\chi}} + \frac{5\sqrt{2}}{2}$, as a function of $\sqrt{\tilde{\chi}}$.

Fig. 6(b), leads to the following fit for $\tilde{\chi}^{1/2} > 200$:

$$\tilde{\sigma} = S_1\tilde{\chi} + S_2\tilde{\chi}^{1/2} + S_3, \tag{29}$$

where $S_1 = (9.765 \pm 0.001) \times 10^{-4}$, $S_2 = -(3.124 \pm 0.004) \times 10^{-2}$, and $S_3 = -0.314 \pm 0.031$.

Motivation for the scaling (26)–(29) based on the asymptotic expansion is presented in Appendix A. The results obtained from the asymptotic expansion lead to the scaling [see Eq. (A4)]

$$k = \frac{\sqrt{2}}{8}\tilde{\chi}^{1/2} + O(1), \tag{30}$$

$$\xi = -\frac{1}{8}\tilde{\chi}^{1/2} + O(1), \tag{31}$$

$$\tilde{\sigma} = \frac{1}{2^{10}}\tilde{\chi} - \frac{1}{2^5}\tilde{\chi}^{1/2} + O(1), \tag{32}$$

which correctly reproduces the slopes of the curves in Fig. 6. The reasoning is limited to values of the arclength s close to the middle of the filament.

IV. THE ELASTICA EIGENFUNCTIONS

A. Local curvature

To analyze the eigenfunctions for the linearized elastica equation, we use the local curvature $\kappa(s)/\max_s \kappa(s)$, defined in Sec. II D. The reason for this choice is that the local curvature is related to the fiber bending energy.

For a wide range of large values of $\tilde{\chi}$, the local curvature is shown by different colors in Fig. 7 separately for the even and odd most unstable eigenfunctions. We observe an increasing number of local maxima for an increasing value of $\tilde{\chi}$, as in Fig. 12 from Ref. [39]. This tendency will be analyzed more precisely in the next section.

B. Scaling of the characteristic wave number

We now perform the fast Fourier transform of the local curvature of the most unstable even and odd eigenfunctions, determined numerically with the Chebyshev spectral collocation method [37,47]. We plot the resulting wave number k in Fig. 8, now as a function of $\sqrt{\tilde{\chi}}$, in a range of $\tilde{\chi} \gg 1$. The colors indicate the intensity of the fast Fourier transform (FFT), divided by its maximum value. For large values of $\tilde{\chi}$, we find that k is a linear function of $\sqrt{\tilde{\chi}}$.

It seems straightforward to compare this linear relation with the dependence on $\sqrt{\tilde{\chi}}$ of the wave vector k in the Gaussian wave packet approximation to the most unstable even and odd eigenvalues, determined in Eqs. (27) and (A4).

However, we should keep in mind that there is a small difference between the dominant wave numbers for $\kappa(s)$ and the corresponding eigenfunction $\Phi(s)$. This difference, discussed in Appendix B, is approximated as a shift up by $2\sqrt{2}$ from the wave number in Eq. (A4), corresponding to the Gaussian wave packet approximation, to the wave number in Eq. (B5), corresponding to the local curvature of the Gaussian wave packet approximation. Therefore, the red line in Fig. 8 corresponds to Eq. (B5). This approximation agrees reasonably well the FFT transform of the local curvature of the numerically evaluated eigenfunctions, with a small systematic difference.

In Appendix C, we compare the local curvature of the eigenfunctions of the elastica linear equation with the numerically found local curvature of an elastic fiber made of beads. The fiber slightly buckled while moving under compression of the shear flow in the time-dependent numerical simulations taking into account the nonzero thickness and hydrodynamic interactions between all the beads using the multipole method [41,42]. The profile of local curvature obtained in the simulations (see Fig. 10) qualitatively matches the results presented in Fig. 7. In particular, we observe an increase in the characteristic wave number with the increase of $\tilde{\chi}$. However, in the case of simulations, for larger values of $\tilde{\chi}$, the increase is moderately slower than for the elastica.

V. CONCLUSIONS

We analyzed the stability of small deformations of a slender elastic fiber in the shear flow (1) of a very viscous fluid by solving the spectral problem for the linearized elastica equations. The infinitely thin fiber is close to straight at an arbitrary 3D orientation, with the perturbations in two perpendicular directions. Even though the spectral differential equations for both perturbations are coupled with each other, we showed that patterns of 3D buckling of elastica are described by one ordinary differential equation with a single parameter, $\tilde{\chi}$. It happens that this equation is the same as that found in [38] for the pure compressional flow but with shifted and rescaled eigenvalues and eigenfunctions. We analyzed the eigenvalues and eigenfunctions for the odd and even modes.

For very flexible fibers, with $\tilde{\chi} \gtrsim 1.5 \times 10^4$, we proposed a wave packet approximation to the most unstable eigenfunctions and showed that it is very accurate. We derived the eigenvalues as linear functions of $\tilde{\chi}$ and the wave packet parameters as linear functions of $\sqrt{\tilde{\chi}}$.

We also analyzed the local curvature of the eigenfunctions, determined numerically by the Chebyshev spectral method [37,47]. By taking the fast Fourier transform of it, we demonstrated the linear scaling of the characteristic wave number with $\sqrt{\tilde{\chi}}$.

The scaling of the buckled shapes and of the instability-growth time derived here might be used to predict and describe the buckling of elastic microfilaments in fluid flows [10,26–33], with possible new applications.

ACKNOWLEDGMENTS

We thank Prof. H. A. Stone for helpful discussions and Prof. D. Saintillan for a useful remark. P.Z. and M.L.E.-J. were supported in part by the National Science Centre under Grant No. UMO-2021/41/B/ST8/04474.

APPENDIX A: MOTIVATION FOR THE SCALING BASED ON THE ASYMPTOTIC EXPANSION

We can benefit from a fiber shape approximated as a wave packet to gain some understanding of the scaling presented in Sec. III. Without loss of generality, we restrict ourselves to the odd approximated solutions from Eq. (26). We are interested in a situation where s is small and $\tilde{\chi}$ is simultaneously large.

We substitute $\Phi = \sin(ks)\exp(\xi s^2)$ on the left side of Eq. (24) and expand the result in powers of s. The left-hand side of Eq. (24) obtained during this procedure has the form

$$s\left(-k^5 + 20k^3\xi - 60k\xi^2 + k\tilde{\chi} + \frac{k^3\tilde{\chi}}{16} - \frac{3k\xi\tilde{\chi}}{8} - k\tilde{\sigma}\tilde{\chi}\right) + s^3\left(\frac{k^7}{6} - 7k^5\xi + 70k^3\xi^2 - 140k\xi^3 - \frac{3k^3\tilde{\chi}}{4} - \frac{k^5\tilde{\chi}}{96} + \frac{9k\xi\tilde{\chi}}{2} + \frac{5k^3\xi\tilde{\chi}}{8} + \frac{k^3\tilde{\sigma}\tilde{\chi}}{6} - k\xi\tilde{\sigma}\tilde{\chi}\right) + O(s^5). \quad \text{(A1)}$$

Moreover, we postulate that k, ξ, and $\tilde{\sigma}$ have the following dependence on $\tilde{\chi} \gg 1$ [this assumption is guided by the numerical fits in Eqs. (27)–(29)]:

$$k = \sum_{j=1}^{\mathcal{N}} K_j \tilde{\chi}^{(2-j)/2}, \quad \xi = \sum_{j=1}^{\mathcal{N}} M_j \tilde{\chi}^{(2-j)/2}, \quad \tilde{\sigma} = \sum_{j=1}^{\mathcal{N}} S_j \tilde{\chi}^{(3-j)/2}, \quad \text{(A2)}$$

where $\mathcal{N}$ is the integer at which we truncate the expansions. In the resulting expansion of expression (A1), the leading terms in $\tilde{\chi}$ for the given power of s are proportional to $\tilde{\chi}^{(2n+3)/2}s^{2n-1}$, where $n = 1, 2, \ldots$. On the other hand, subleading terms are analogously commensurate with $\tilde{\chi}^{(2n+3-m)/2}s^{2n-1}$, where $m = 1, 2, \ldots, m_{\max}$ indexes consecutive terms in the expansion in powers of $\tilde{\chi}^{-1/2}$. The parameter $m_{\max}$ grows with values of n and $\mathcal{N}$ (see Table I). The dependence of $m_{\max}$ on n and $\mathcal{N}$ can be expressed using the formula

$$m_{\max} = \begin{cases} n+1, & \text{for } \mathcal{N} = 1, \\ (2n+3)2^{\mathcal{N}-2}, & \text{for } \mathcal{N} > 1. \end{cases} \quad \text{(A3)}$$

The parameter $m_{\max}$ indicates the number of subleading terms for the expansion's given cutoff value $\mathcal{N}$ and the power of s equal to $2n-1$.

We illustrate the procedure for finding the values of the coefficients in Eq. (A2) for the truncation at $\mathcal{N} = 1$. The terms of the expansion for $\mathcal{N} = 1$ are schematically presented in Table II, e.g., a cell for $n = 2$ and $m = 1$ represents the term for order $s^3\tilde{\chi}^3$, and we similarly interpret other terms.

TABLE I. Values of parameter $m_{\max}$ as a function of n and $\mathcal{N}$.

	$n=1$	$n=2$	$n=3$	$n=4$	$n=5$	...
$\mathcal{N}=1$	2	3	4	5	6	...
$\mathcal{N}=2$	5	7	9	11	13	...
$\mathcal{N}=3$	10	14	18	22	26	...
$\mathcal{N}=4$	20	28	36	44	52	...
⋮	⋮	⋮	⋮	⋮	⋮	⋱

TABLE II. Terms in the expansion (A2) of expression (A1).

		$m=0$	$m=1$	$m=2$	$m=3$	...
$n=1$	s^1	$\tilde{\chi}^{5/2}$	$\tilde{\chi}^{2}$	$\tilde{\chi}^{3/2}$		
$n=2$	s^3	$\tilde{\chi}^{7/2}$	$\tilde{\chi}^{3}$	$\tilde{\chi}^{5/2}$	$\tilde{\chi}^{2}$	
$n=3$	s^5	$\tilde{\chi}^{9/2}$	$\tilde{\chi}^{4}$	$\tilde{\chi}^{7/2}$	$\tilde{\chi}^{3}$	$\tilde{\chi}^{5/2}$
⋮	⋮	⋮	⋮	⋮	⋮	⋱

TABLE III. Values of the expansion coefficients for the parameters k, ξ, and $\tilde{\sigma}$ for $\mathcal{N} = 1, 2, 3, 4$ obtained from the asymptotic expansion. The results are compared with the fitting results from the Eqs. (27)–(29).

	K_1	K_2	
$\mathcal{N} = 1$	0.137		
$\mathcal{N} = 2$	0.177	-0.131	
$\mathcal{N} = 3$	0.177	0.707	
$\mathcal{N} = 4$	0.177	0.707	
Fitted values	0.176	-0.249	
	M_1	M_2	
$\mathcal{N} = 1$	-0.129		
$\mathcal{N} = 2$	-0.137	2.929×10^{-3}	
$\mathcal{N} = 3$	-0.125	-3.5	
$\mathcal{N} = 4$	-0.125	-3.5	
Fitted values	-0.124	0.417	
	S_1	S_2	S_3
$\mathcal{N} = 1$	8.203×10^{-4}		
$\mathcal{N} = 2$	9.765×10^{-4}	-3.424×10^{-2}	
$\mathcal{N} = 3$	9.765×10^{-4}	-3.125×10^{-2}	-1.75
$\mathcal{N} = 4$	9.765×10^{-4}	-3.125×10^{-2}	-1.75
Fitted values	9.765×10^{-4}	-3.124×10^{-2}	-0.314

We must find the values of K_1, M_1, and S_1. Thus, we demand that coefficient for terms of leading orders $s^1\tilde{\chi}^{5/2}$, $s^1\tilde{\chi}^2$, and $s^1\tilde{\chi}^{3/2}$ ($n = 1$, green online) should identically be equal to zero, which leads to values of $K_1 = \frac{1}{4}\sqrt{\frac{3}{10}}$, $M_1 = -\frac{1}{2\sqrt{15}}$, and $S_1 = \frac{21}{25600}$. When the equation for order $s^1\tilde{\chi}^{5/2}$ is satisfied, then the dominant contributions for higher powers of s, i.e., $s^3\tilde{\chi}^{7/2}$, $s^5\tilde{\chi}^{9/2}$, ... ($n > 1$ and $m = 0$, violet online), are vanishing. This is true for any value of $\mathcal{N}$ because these coefficients have the same form as that for order $s^1\tilde{\chi}^{5/2}$ multiplied by a number and some power of K_1. Moreover, when we restrict ourselves to $s = o(\tilde{\chi}^{-1})$ (see, e.g., [48]), all other terms in the expansion ($n > 1$ and $m > 0$, pink online) asymptotically go to zero.

Similarly, one can obtain more accurate results for truncation at larger values of $\mathcal{N}$, but it complicates calculations. A higher value of $\mathcal{N}$ allows the application of less restrictive requirements for the asymptotic behavior of s, i.e., $s = o(\tilde{\chi}^{-\zeta})$, where $\zeta < 1$ and $\zeta \to 0^+$ for $\mathcal{N} \to \infty$. In Table III, we compare the asymptotic expansion results for the parameters k, ξ, and $\tilde{\sigma}$ for four successive values of $\mathcal{N}$. Table III also provides the Gaussian wave packet fitting results discussed in Sec. III B. We also present a comparison of Eqs. (27), (28), (29), and (A4) in Fig. 9. The results presented in Table III show that the values of the expansion coefficients stabilize for $\mathcal{N} \geqslant 3$.

We finally take $\mathcal{N} = 4$ and obtain the following expressions for k, ξ, and $\tilde{\sigma}$:

$$k = \frac{\sqrt{2}}{8}\tilde{\chi}^{1/2} + \frac{\sqrt{2}}{2} + O(\tilde{\chi}^{-1/2}),$$
$$\xi = -\frac{1}{8}\tilde{\chi}^{1/2} - \frac{9}{2} + O(\tilde{\chi}^{-1/2}),$$
$$\tilde{\sigma} = \frac{1}{2^{10}}\tilde{\chi} - \frac{1}{2^5}\tilde{\chi}^{1/2} - \frac{7}{4} + O(\tilde{\chi}^{-1/2}). \quad \text{(A4)}$$

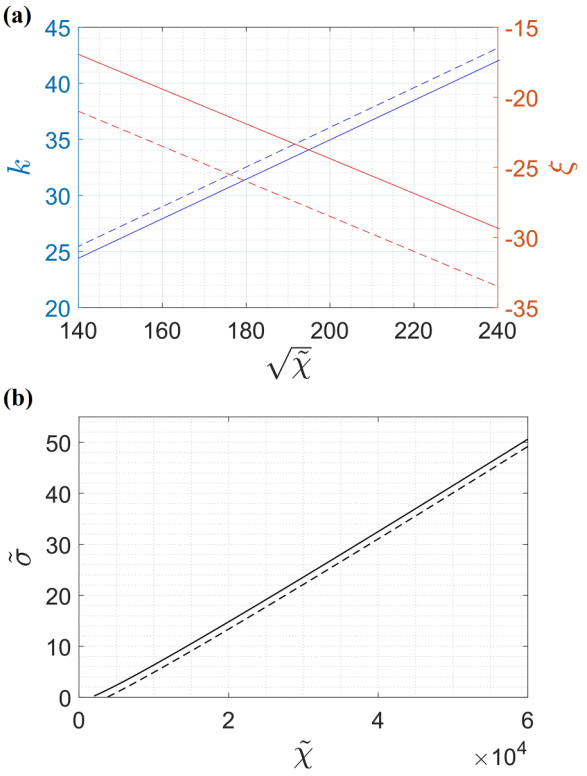

FIG. 9. Comparison of the parameters k, ξ, and $\tilde{\sigma}$ as a function of $\tilde{\chi}$ obtained by fitting a Gaussian wave packet [solid line, see Eqs. (27)–(29) and Table III] and asymptotic expansion with $\mathcal{N} = 4$ [dashed line, see Eq. (A4)]. The analytical results accurately reproduce the slopes of the curves.

For $\mathcal{N}$=4, we assume that $s = o(\tilde{\chi}^{-4/7})$, which guarantees that higher order terms in the expansion in powers of s and $\tilde{\chi}$ asymptotically vanish. As one can see by comparing Eqs. (27)–(29) with Eq. (A4), our analytical coefficients in Eq. (A4) are approximated with excellent accuracy by the coefficients K_1, M_1, S_1, and S_2 obtained from the numerical fit in Eqs. (27)–(29).

The asymptotic expansion presented above works for small values of s. However, the numerical fit demonstrates that the wave packet (26) with the parameters (A4) well approximates the eigenfunctions and eigenvalues in the whole range of s.

APPENDIX B: WAVE NUMBERS BASED ON SHAPE AND CURVATURE

The Fourier transform $F(\alpha)$ of a function $f(s)$ is defined as

$$F_f(\alpha) = \int_{-\infty}^{+\infty} f(s)\exp^{-is\alpha}\, ds. \quad \text{(B1)}$$

For the wave packet $\Phi(s)$ given by Eqs. (26) and (A4), the Fourier transform scales as

$$F_\Phi(\alpha) \propto \exp[(\alpha - k)^2/(4\xi)], \quad \text{(B2)}$$

with the maximum of $F_\Phi(\alpha)$ at

$$\alpha = \alpha_0 = k \approx \frac{\sqrt{2}}{8}(\sqrt{\tilde{\chi}} + 4). \quad \text{(B3)}$$

The Fourier transform of the curvature, approximated as $\kappa'(s) \propto -d^2\Phi(s)/ds^2$, scales as

$$F_{\kappa'}(\alpha) \propto \alpha^2 \exp[(\alpha - k)^2/(4\xi)]. \tag{B4}$$

Calculating zeros of the derivative and using Eq. (A4), we determine that the maximum of $F_{\kappa'}(\alpha)$ is located at

$$\alpha = \alpha_1 \approx \frac{k}{2}\left(1 + \sqrt{1 - \frac{16\xi}{k^2}}\right) \approx k - \frac{4\xi}{k} \approx \alpha_0 + 2\sqrt{2}$$
$$\approx \frac{\sqrt{2}}{8}\sqrt{\tilde{\chi}} + \frac{5\sqrt{2}}{2}. \tag{B5}$$

In Eq. (B5), we demonstrate that the wave numbers α_0 and α_1, based on shape and curvature, respectively, are not the same and $\alpha_1 > \alpha_0$. Within the adopted approximation, they are both linear functions of $\sqrt{\tilde{\chi}}$ with the same slope but shifted with respect to each other. A more precise relation would be obtained if terms $\propto 1/\sqrt{\tilde{\chi}}$ were taken into account. In this case, α_1 would be a nonlinear function of $\sqrt{\tilde{\chi}}$.

The curvature κ used earlier is related to κ' by the equation $\kappa = |\kappa'|$. Therefore, the characteristic wave number for κ is $2\alpha_1$.

APPENDIX C: EVOLUTION OF AN ELASTIC FILAMENT WITH A NON-NEGLIGIBLE THICKNESS

In this Appendix, we compare the local curvature of the elastica eigenfunctions with the local curvature of an elastic fiber with a non-negligible thickness, taking into account hydrodynamic interactions between all the fiber segments in the shear flow.

Following previous publications [39,49–51], we use the bead model. An elastic filament of thickness d is modeled as a chain of $N = 40$ identical, spherical, solid beads with diameter d. Consecutive beads are connected by springs with the spring constant $\mathcal{K}$, and the equilibrium distance between the bead centers (the bond length) is equal to $\ell_0 = 1.02d$. Consecutive bonds are also connected by springs, with the bending stiffness

$$\mathcal{A} = E\pi d^4/64, \tag{C1}$$

where E is Young's modulus. At the elastic equilibrium, the fiber is straight. The stretching and bending potential energies of the filament are

$$E_s = \frac{\mathcal{K}}{2}\sum_{i=2}^{N}(\ell_i - \ell_0)^2, \quad E_b = \frac{\mathcal{A}}{2\ell_0}\sum_{i=2}^{N-1}\beta_i^2, \tag{C2}$$

with $\ell_i = |\boldsymbol{\mathcal{R}}_i - \boldsymbol{\mathcal{R}}_{i-1}|$, where $\boldsymbol{\mathcal{R}}_i$ is the position of the center of bead i and

$$\cos\beta_i = (\boldsymbol{\mathcal{R}}_i - \boldsymbol{\mathcal{R}}_{i-1}) \cdot (\boldsymbol{\mathcal{R}}_{i+1} - \boldsymbol{\mathcal{R}}_i)/(\ell_i\ell_{i+1}). \tag{C3}$$

Taking d and $1/\dot{\gamma}$ as the length and time units, respectively, the dimensionless quantities are $\boldsymbol{r}_i = \boldsymbol{\mathcal{R}}_i/d$, $k_0 = \mathcal{K}/(\pi\mu d\dot{\gamma})$, and $A = E/(64\mu\dot{\gamma})$. The filaments are almost inextensible, $k_0 = 1000$, and their bending stiffness ratio $A \in [20, 1000]$.

The dynamics of the no-slip beads are evaluated from the Stokes equations by the multipole expansion, as in [52,53], corrected for lubrication and implemented in the precise HYDROMULTIPOLE numerical code, as described in Refs. [41,42]. As in Refs. [24,39,51,54], positions $\boldsymbol{r}_i$ of the bead centers satisfy the following equations:

$$\dot{\boldsymbol{r}}_i - \boldsymbol{v}_0(\boldsymbol{r}_i) = \sum_{j=1}^{N}\left(\boldsymbol{\mu}_{ij}^{tt} \cdot \boldsymbol{F}_j + \boldsymbol{\mu}_{ij}^{td} : \boldsymbol{E}_\infty\right), \quad i = 1, \ldots, N, \tag{C4}$$

where

$$\boldsymbol{F}_j = \frac{1}{\pi\mu d^3\dot{\gamma}}\frac{\partial}{\partial \boldsymbol{r}_j}(E_s + E_b) \tag{C5}$$

is the dimensionless elastic force acting on the bead j and

$$\mathbf{E}_\infty = \tfrac{1}{2}[\nabla \boldsymbol{v}_0 + (\nabla \boldsymbol{v}_0)^T] \tag{C6}$$

is the rate-of-strain tensor. The mobility matrices, $\boldsymbol{\mu}_{ij}^{tt}$ and $\boldsymbol{\mu}_{ij}^{td}$, depend on the positions of all the bead centers and are evaluated by the HYDROMULTIPOLE program, with the multipole truncation order $L = 2$. In Ref. [51] the approximation of $L = 2$ was compared with the approximations of $L = 3$ and $L = 4$, and it was shown that the difference is of the order of 2%, and therefore, $L = 2$ is sufficiently accurate (while much faster than higher values of L).

In Ref. [39] numerical simulations of initially straight elastic fibers were performed and obtained only odd buckled shapes. This result is caused by the fiber thickness, which promotes odd deformation. To observe even shapes, an even initial perturbation is needed, as in the numerical simulation in Ref. [12]. Therefore, in this paper, we initially impose a small, but significant, either odd or even perturbation of the center of bead i relative to the center of a straight fiber in elastic equilibrium, oriented at $\theta_0 = 90^\circ$ and $\phi_0 = 160^\circ$. The perturbation does not depend on A and is restricted to the shear plane $\delta_i(-\sin\phi_0, \cos\phi_0, 0)$, with

$$\delta_i = a\sum_{m=1}^{5}\frac{(-1)^{q_m}}{(2m)^2}\sin\left[2m\pi\left(\frac{i-1}{N-1} - \frac{1}{2}\right)\right] \tag{C7}$$

for the odd perturbation, where q_m are independent random variables equal to 1 or 2 with a probability of 1/2. Finally, the positions are shifted to make all the distances between the bead centers equal to the equilibrium value $\ell_0/d = 1.02$. The value of a is chosen so that the maximum distance of a bead center from the unperturbed filament is $d_m \approx 0.076$. The even initial perturbation is constructed similarly, with $d_m \approx 0.19$. Both initial perturbations of all the beads are listed in an open repository [55].

We compare an elastic filament of length L and diameter d, made of $N = 40$ beads, to the elastica with $L/d \approx 40$ and the same value of Young's modulus E. Therefore, Eq. (3) and the relation

$$A = \frac{E}{64\mu\dot{\gamma}} \tag{C8}$$

determine η as a function of A,

$$\eta = \frac{2}{\ln(2L/d)}\left(\frac{L}{d}\right)^4 A^{-1} = 1.17 \times 10^6 A^{-1}. \tag{C9}$$

In the simulations, for each A we select the filament shape at time $t = 0.75$, sufficient for the development of the buckling instability and small enough for a small change in the angle ϕ of the filament principal axis, as shown in Ref. [39]

in Fig. 13. Then, we compare it with the most unstable eigenfunction of the same parity $\Phi_{u1}(\tilde{\chi})$, where

$$\tilde{\chi} = -\eta \sin(2\phi_0) \sin^2\theta_0 = 7.5 \times 10^5 A^{-1}. \tag{C10}$$

To analyze the filament shapes, we use the local curvature. At the center of bead $i = 2, \ldots, N-1$ it is given as

$$\kappa_i = \frac{2|(\boldsymbol{r}_{i-1} - \boldsymbol{r}_i) \times (\boldsymbol{r}_i - \boldsymbol{r}_{i+1})|}{|\boldsymbol{r}_{i-1} - \boldsymbol{r}_i||\boldsymbol{r}_i - \boldsymbol{r}_{i+1}||\boldsymbol{r}_{i+1} - \boldsymbol{r}_{i-1}|}. \tag{C11}$$

We use $s_i = -0.5 + (i-1)/(N-1)$ as a discrete analog of the arclength s. Then, s_i and κ_i are interpolated, and κ_i is normalized by its maximum value along the filament.

The local curvature as a function of s_i and $\tilde{\chi}$ is shown by different colors in Fig. 10 separately for the even and odd initial perturbations. We observe that at $t = 0.75$, the parity of the filament shapes is the same as the parity of the initial perturbation. The dependence of the fiber shape on $\tilde{\chi}$, shown in Fig. 10, is very similar to that in the case of the elastica, shown in Fig. 7. For large values of $\tilde{\chi}$, the models agree with each other qualitatively. We observe an increasing number of the local maxima of the fiber curvature for increasing values of $\tilde{\chi}$, as in Fig. 12 in Ref. [39], corresponding to the increase in the characteristic wave number. For large values of $\tilde{\chi}$, the increase in the wave number of an elastic filament made of beads is slightly slower than that of the elastica.

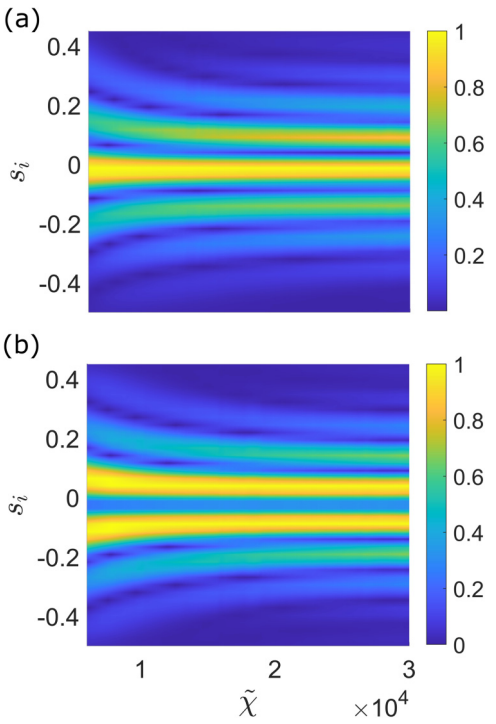

FIG. 10. Local curvature of an elastic filament, normalized by its maximum value along the filament and shown as different colors. Numerical simulations for the elastic filament made of beads at $t = 0.75$ for the initially almost straight configuration oriented at the angles $\theta_0 = 90^\circ$ and $\phi_0 = 160^\circ$, with (a) even and (b) odd initial perturbations.

[1] M. J. Shelley and J. Zhang, Flapping and bending bodies interacting with fluid flows, Annu. Rev. Fluid Mech. **43**, 449 (2011).

[2] A. Lindner and M. J. Shelley, Elastic fibers in flows, in *Fluid-Structure Interactions in Low Reynolds Number Flows*, edited by C. Duprat and H. A. Stone (Royal Society of Chemistry, Cambridge, 2015), pp. 168–189.

[3] O. du Roure, A. Lindner, E. N. Nazockdast, and M. J. Shelley, Dynamics of flexible fibers in viscous flows and fluids, Annu. Rev. Fluid Mech. **51**, 539 (2019).

[4] T. A. Witten and H. Diamant, A review of shaped colloidal particles in fluids: Anisotropy and chirality, Rep. Prog. Phys. **83**, 116601 (2020).

[5] H. C. Berg and R. A. Anderson, Bacteria swim by rotating their flagellar filaments, Nature (London) **245**, 380 (1973).

[6] C. W. Wolgemuth, N. W. Charon, S. F. Goldstein, and R. E. Goldstein, The flagellar cytoskeleton of the spirochetes, J. Mol. Microbiol. **11**, 221 (2006).

[7] R. E. Goldstein, M. Polin, and I. Tuval, Noise and synchronization in pairs of beating eukaryotic flagella, Phys. Rev. Lett. **103**, 168103 (2009).

[8] M. M. Musielak, L. Karp-Boss, P. A. Jumars, and L. J. Fauci, Nutrient transport and acquisition by diatom chains in a moving fluid, J. Fluid Mech. **638**, 401 (2009).

[9] M. Garcia, S. Berti, P. Peyla, and S. Rafaï, Random walk of a swimmer in a low-Reynolds-number medium, Phys. Rev. E **83**, 035301(R) (2011).

[10] V. Kantsler and R. E. Goldstein, Fluctuations, dynamics, and the stretch-coil transition of single actin filaments in extensional flows, Phys. Rev. Lett. **108**, 038103 (2012).

[11] M. Harasim, B. Wunderlich, O. Peleg, M. Kröger, and A. R. Bausch, Direct observation of the dynamics of semiflexible polymers in shear flow, Phys. Rev. Lett. **110**, 108302 (2013).

[12] Y. Liu, B. Chakrabarti, D. Saintillan, A. Lindner, and O. du Roure, Morphological transitions of elastic filaments in shear flow, Proc. Natl. Acad. Sci. USA **115**, 9438 (2018).

[13] K. M. Kenitz, E. C. Orenstein, P. L. Roberts, P. J. Franks, J. S. Jaffe, M. L. Carter, and A. D. Barton, Environmental drivers of population variability in colony-forming marine diatoms, Limnol. Oceanogr. **65**, 2515 (2020).

[14] D. H. Reneker and A. L. Yarin, Electrospinning jets and polymer nanofibers, Polymer **49**, 2387 (2008).

[15] J. K. Nunes, H. Constantin, and H. A. Stone, Microfluidic tailoring of the two-dimensional morphology of crimped microfibers, Soft Matter **9**, 4227 (2013).
[16] P. Nakielski *et al.*, Multifunctional platform based on electrospun nanofibers and plasmonic hydrogel: A smart nanostructured pillow for near-infrared light-driven biomedical applications, ACS Appl. Mater. Interfaces **12**, 54328 (2020).
[17] S. Yamamoto and T. Matsuoka, A method for dynamic simulation of rigid and flexible fibers in a flow field, J. Chem. Phys. **98**, 644 (1993).
[18] P. Skjetne, R. F. Ross, and D. J. Klingenberg, Simulation of single fiber dynamics, J. Chem. Phys. **107**, 2108 (1997).
[19] A.-K. Tornberg and M. J. Shelley, Simulating the dynamics and interactions of flexible fibers in Stokes flows, J. Comput. Phys. **196**, 8 (2004).
[20] N. Autrusson, L. Guglielmini, S. Lecuyer, R. Rusconi, and H. A. Stone, The shape of an elastic filament in a two-dimensional corner flow, Phys. Fluids **23**, 063602 (2011).
[21] A. Farutin, T. Piasecki, A. M. Słowicka, C. Misbah, E. Wajnryb, and M. L. Ekiel-Jeżewska, Dynamics of flexible fibers and vesicles in Poiseuille flow at low Reynolds number, Soft Matter **12**, 7307 (2016).
[22] H. Nguyen and L. Fauci, Hydrodynamics of diatom chains and semiflexible fibres, J. R. Soc. Interface **11**, 20140314 (2014).
[23] J. LaGrone, R. Cortez, W. Yan, and L. Fauci, Complex dynamics of long, flexible fibers in shear, J. Non-Newtonian Fluid Mech. **269**, 73 (2019).
[24] P. J. Żuk, A. M. Słowicka, M. L. Ekiel-Jeżewska, and H. A. Stone, Universal features of the shape of elastic fibres in shear flow, J. Fluid Mech. **914**, A31 (2021).
[25] C. Kurzthaler, R. Brandão, O. Schnitzer, and H. A. Stone, Shape of a tethered filament in various low-Reynolds-number flows, Phys. Rev. Fluids **8**, 014101 (2023).
[26] Y.-N. Young and M. J. Shelley, Stretch-coil transition and transport of fibers in cellular flows, Phys. Rev. Lett. **99**, 058303 (2007).
[27] E. Wandersman, N. Quennouz, M. Fermigier, A. Lindner, and O. du Roure, Buckled in translation, Soft Matter **6**, 5715 (2010).
[28] L. Guglielmini, A. Kushwaha, E. Shaqfeh, and H. A. Stone, Buckling transitions of an elastic filament in a viscous stagnation point flow, Phys. Fluids **24**, 123601 (2012).
[29] H. Manikantan and D. Saintillan, Buckling transition of a semiflexible filament in extensional flow, Phys. Rev. E **92**, 041002(R) (2015).
[30] N. Quennouz, M. Shelley, O. du Roure, and A. Lindner, Transport and buckling dynamics of an elastic fibre in a viscous cellular flow, J. Fluid Mech. **769**, 387 (2015).
[31] A. L. Hall-McNair, T. D. Montenegro-Johnson, H. Gadêlha, D. J. Smith, and M. T. Gallagher, Efficient implementation of elastohydrodynamics via integral operators, Phys. Rev. Fluids **4**, 113101 (2019).
[32] M. Kanchan and R. Maniyeri, Numerical analysis of the buckling and recuperation dynamics of flexible filament using an immersed boundary framework, Int. J. Heat Fluid Flow **77**, 256 (2019).
[33] C. Marchioli and D. Di Giusto, Slender flexible fibers in turbulent channel flow, Bull. Am. Phys. Soc. **68**, X46.00011 (2023).
[34] O. L. Forgacs and S. G. Mason, Particle motions in sheared suspensions: IX. Spin and deformation of threadlike particles, J. Colloid Sci. **14**, 457 (1959).
[35] O. L. Forgacs and S. G. Mason, Particle motions in sheared suspensions: X. Orbits of flexible threadlike particles, J. Colloid Sci. **14**, 473 (1959).
[36] L. E. Becker and M. J. Shelley, Instability of elastic filaments in shear flow yields first-normal-stress differences, Phys. Rev. Lett. **87**, 198301 (2001).
[37] L. Liu, P. Sznajder, and M. L. Ekiel-Jeżewska, Spectral analysis for elastica dynamics in a shear flow, Phys. Rev. Fluids **9**, 014101 (2024).
[38] B. Chakrabarti, Y. Liu, J. LaGrone, R. Cortez, L. Fauci, O. du Roure, D. Saintillan, and A. Lindner, Flexible filaments buckle into helicoidal shapes in strong compressional flows, Nat. Phys. **16**, 689 (2020).
[39] A. M. Słowicka, N. Xue, P. Sznajder, J. K. Nunes, H. A. Stone, and M. L. Ekiel-Jeżewska, Buckling of elastic fibers in a shear flow, New J. Phys. **24**, 013013 (2022).
[40] B. Audoly and Y. Pomeau, Elasticity and geometry, in *Peyresq Lectures on Nonlinear Phenomena* (World Scientific, Singapore, 2000), pp. 1–35.
[41] B. Cichocki, M. L. Ekiel-Jeżewska, and E. Wajnryb, Lubrication corrections for three-particle contribution to short-time self-diffusion coefficients in colloidal dispersions, J. Chem. Phys. **111**, 3265 (1999).
[42] M. L. Ekiel-Jeżewska and E. Wajnryb, Precise multipole method for calculating hydrodynamic interactions between spherical particles in the Stokes flow, in *Theoretical Methods for Micro Scale Viscous Flows*, edited by F. Feuillebois and A. Sellier (Transworld Research Network, Kerala, India, 2009), pp. 127–172.
[43] B. Audoly, Introduction to the elasticity of rods, in *Fluid-Structure Interactions in Low-Reynolds-Number Flows*, edited by C. Duprat and H. A. Stone (Royal Society of Chemistry, 2015), pp. 1–24.
[44] G. Batchelor, Slender-body theory for particles of arbitrary cross-section in Stokes flow, J. Fluid Mech. **44**, 419 (1970).
[45] E. Lauga and T. R. Powers, The hydrodynamics of swimming microorganisms, Rep. Prog. Phys. **72**, 096601 (2009).
[46] H. A. Stone and C. Duprat, Low-Reynolds-number flows, in *Fluid-Structure Interactions in Low-Reynolds-Number Flows*, edited by C. Duprat and H. A. Stone (Royal Society of Chemistry, 2015), pp. 25–77.
[47] L. Liu, P. Sznajder, and M. L. Ekiel-Jeżewska, Eigenfunctions and eigenvalues for elastica in a shear flow, Repository for Open Data (2023), doi: 10.18150/USFQAK.
[48] H. Jeffreys and B. Jeffreys, *Methods of Mathematical Physics*, Cambridge Mathematical Library (Cambridge University Press, Cambridge, 1999).
[49] B. Delmotte, E. Climent, and F. Plouraboué, A general formulation of bead models applied to flexible fibers and active filaments at low Reynolds number, J. Comput. Phys. **286**, 14 (2015).
[50] E. Gauger and H. Stark, Numerical study of a microscopic artificial swimmer, Phys. Rev. E **74**, 021907 (2006).
[51] A. M. Słowicka, E. Wajnryb, and M. L. Ekiel-Jeżewska, Dynamics of flexible fibers in shear flow, J. Chem. Phys. **143**, 124904 (2015).

[52] B. U. Felderhof, Many-body hydrodynamic interactions in suspensions, Phys. A (Amsterdam, Neth.) **151**, 1 (1988).

[53] S. Kim and S. Karrila, *Microhydrodynamics: Principles and Selected Applications* (Butterworth-Heinemann, Boston and London, 1991).

[54] A. M. Słowicka, H. A. Stone, and M. L. Ekiel-Jeżewska, Flexible fibers in shear flow approach attracting periodic solutions, Phys. Rev. E **101**, 023104 (2020).

[55] P. Sznajder, P. Zdybel, L. Liu, and M. Ekiel-Jeżewska, Initial configurations of elastic fibers, Repository for Open Data (2024), doi: 10.18150/P442KP.